

Computational and Experimental Investigation of Fan Flow Deflection for Supersonic Turbofan Engines

Juntao Xiong¹, Preben Nielsen², Feng Liu³ and Dimitri Papamoschou⁴
University of California, Irvine, CA 92697, USA

We present a combined experimental and computational study of the dual-stream exhaust of a supersonic turbofan engine with noise-suppressing deflectors installed in the fan stream. The focus is on validating the computational code, extracting turbulent kinetic energy (TKE) trends, and connecting those trends to the measured noise reduction. We consider two operating conditions, a “cold” condition at which mean flow surveys were conducted and against which the code was validated; and a “hot” condition that corresponds to the takeoff engine cycle and at which acoustic measurements were conducted. A three-dimensional Reynolds-Averaged Navier Stokes code is used to simulate the flow for a number of nozzle configurations using vane type flow deflectors to create asymmetric jet plumes, which have demonstrated experimentally the potential for significant noise reduction. The code successfully replicates the mean velocity, radial velocity gradient and inflectional layer fields of the experimental flows. Comparison of “cold” and “hot” condition shows a reasonable collapse of the velocity profiles when the axial distance is normalized by the potential core length. For both conditions, the vane deflectors reduce the TKE on the underside of the jet and increase it on the topside of the jet. There is a significant correlation between the decrease of the TKE near the end of the potential core and the reduction in overall sound pressure level in the direction of peak emission. This study will provide a basis for the further use of CFD in the investigation of noise reduction and performance of fan flow deflected supersonic turbofan engines.

Nomenclature

A	= area
c	= chord
D_f	= nozzle fan diameter
E	= total internal energy
F_c	= inviscid convective flux
F_d	= inviscid diffusive flux
G	= radial velocity gradient
k	= turbulent kinetic energy
M	= Mach number
NPR	= nozzle pressure ratio
p	= pressure
r	= radial direction
W	= conservative variable vector
U	= nozzle exit velocity
u, v, w	= velocity components in x, y, z directions
x	= axial direction (from plug tip)
y	= vertical transverse direction
z	= horizontal transverse direction

¹ Post Doctoral Researcher, Department of Mechanical and Aerospace Engineering, jxiong@uci.edu.

² Graduate Researcher, Department of Mechanical and Aerospace Engineering, nielsenp@uci.edu, AIAA Student Member.

³ Professor, Department of Mechanical and Aerospace Engineering, fliu@uci.edu, AIAA Associate Fellow.

⁴ Professor, Department of Mechanical and Aerospace Engineering, dpapamos@uci.edu, AIAA Fellow.

α	= angle of attack
θ	= polar angle from jet axis
μ_L	= molecular viscosity
μ_T	= turbulent viscosity
ρ	= density
τ	= stress tensor
ϕ	= azimuth angle from downward vertical
Ω	= vorticity
ω	= specific dissipation rate

Subscripts

TE	= trailing edge
p	= primary (core) exhaust
PC	= primary core
s	= secondary (fan) exhaust
SC	= secondary core
∞	= free stream
max	= maximum

I. Introduction

Asymmetric distortion of the dual-stream exhaust plume of turbofan engines has previously demonstrated the potential for significant directional noise suppression in both subsonic and supersonic applications^{1,2}. In order to facilitate the study of asymmetric dual-stream jets a computational study has been established which aims to supplement the experimental mean velocity testing of these jets with the vision of using a computational model to predict the noise that will be produced from certain asymmetric flow fields. The purpose of this study is to validate the results of the computational study with experimental results for various dual-stream nozzle configurations that result in exhaust plume asymmetry and to explore correlations between the computed turbulence field and associated noise radiation. The study focuses on supersonic turbofan exhaust, but the results are expected to be general enough to be applicable to subsonic flows as well. In this particular investigation the asymmetry of the plume is created by the use of fan flow deflectors as depicted in Fig. 1.

A simplified model for the distortion of the mean flow field is shown in Fig. 2. The deflection of the fan flow has the potential to introduce three effects on the mean flow, in the general direction of the deflection; elongation of the inflectional layer defined by points i_2 and i_3 of the velocity profile, reduction of the velocity gradient and a contraction of the primary potential core. All these effects are expected to suppress noise. Elongation of the secondary core inflectional layer and/or contraction of the primary potential core prolongs the region of the primary shear layer that is “silenced” by the fan flow. Reduction of the velocity gradient is expected to reduce the production rate for turbulent kinetic energy k . Past experiments⁴ and computations⁵ in dual-stream nozzles with fan flow deflectors have shown reduced values of k on the underside of the jet. Importantly, the experiments have shown a correlation between velocity gradients and k near the end of the potential core of the jet⁴. Given that the jet has a finite axial extent it is thus possible to reduce k throughout the underside of the jet. In turn, reducing k is expected to reduce the noise source. In prevailing empirical jet noise models³ the noise source term dependence on turbulent kinetic energy is as strong as $k^{7/2}$. Previous experiments have shown a significant correlation between reduction in velocity gradients and directional noise suppression from asymmetric dual-stream jets⁶.

This investigation starts with validation of the computational results with experimental measurements of the mean velocity field conducted at “cold” conditions. Once the validation is confirmed, the code is then extended to “hot” conditions corresponding to the actual takeoff engine cycle. A discussion on the comparison between “cold” and “hot” velocity fields is presented. Finally, turbulence data for various fan flow deflection configurations that are computed using the “hot” jet cycle point conditions are presented and correlations are drawn between the turbulent kinetic energy data and the overall sound pressure level (OASPL) that was measured in the acoustic experiments. The computational model in conjunction with experimental data for asymmetric jet plumes are studied to provide insight into the physics of noise production in asymmetric jets and for the development and optimization of asymmetry inducing schemes such as fan flow deflectors.

II. Computational Details

A. Numerical Code

The computational fluid dynamics code used here is known as ParCAE and solves the unsteady three-dimensional Reynolds-averaged Navier-Stokes (RANS) equations on structured multi-block grids using a cell centered finite-volume method with artificial dissipation as proposed by Jameson et al⁷. Information exchange for flow computation on multi-block grids using multiple CPUs is implemented through the MPI (message passing interface) protocol. The RANS equations are solved using the eddy viscosity type turbulence models. The code contains the Baldwin-Lomax algebraic model⁸, one-equation Spapart-Allmaras⁹ turbulence model, two-equation $k-\omega$ model of Wilcox¹⁰ and Menter¹¹ shear stress transport (SST) turbulence model. In this study, only the steady-state solution is obtained because we are interested in the time-averaged features of the flow. The SST turbulence model combines the advantages of the $k-\omega$ and $k-\varepsilon$ turbulence models to give superior performance in simulating the wall boundary layer and free-stream flow, thus the SST model was chosen for all the cases in this work. The main elements of the code are summarized below.

The governing equations for the unsteady compressible turbulent flow with a SST turbulence model are expressed as follows;

$$\frac{\partial}{\partial t} \int_{\Omega} \mathbf{W} d\Omega + \oint_{\partial\Omega} (\mathbf{F}_c - \mathbf{F}_d) dS = \int_{\Omega} \mathbf{S} d\Omega \quad (1)$$

The vector \mathbf{W} contains the conservative variables;

$$\mathbf{W} = \begin{pmatrix} \rho \\ \rho u \\ \rho v \\ \rho w \\ \rho E \\ \rho k \\ \rho \omega \end{pmatrix} \quad (2)$$

The fluxes consist of the inviscid convective fluxes F_c and the diffusive fluxes F_d . For the convective fluxes the pressure term is included;

$$\mathbf{F}_c = \begin{bmatrix} \rho u & \rho v & \rho w \\ \rho u u + p & \rho u v & \rho u w \\ \rho v u & \rho v v + p & \rho v w \\ \rho w u & \rho w v & \rho w w + p \\ \rho E u + p u & \rho E v + p v & \rho E w + p w \\ \rho k u & \rho k v & \rho k w \\ \rho \omega u & \rho \omega v & \rho \omega w \end{bmatrix} \quad (3)$$

The diffusive fluxes are given by;

$$\mathbf{F}_d = \begin{pmatrix} 0 & 0 & 0 \\ \tau_{xx} & \tau_{xy} & \tau_{xz} \\ \tau_{yx} & \tau_{yy} & \tau_{yz} \\ \tau_{zx} & \tau_{zy} & \tau_{zz} \\ \theta_x & \theta_y & \theta_z \\ \mu_k^* \frac{\partial k}{\partial x} & \mu_k^* \frac{\partial k}{\partial y} & \mu_k^* \frac{\partial k}{\partial z} \\ \mu_\omega^* \frac{\partial \omega}{\partial x} & \mu_\omega^* \frac{\partial \omega}{\partial y} & \mu_\omega^* \frac{\partial \omega}{\partial z} \end{pmatrix} \quad (4)$$

where

$$\begin{aligned} \mu_k^* &= \mu_L + \sigma_k \mu_T \\ \mu_\omega^* &= \mu_L + \sigma_\omega \mu_T \\ \mu_T &= \frac{\rho a_1 k}{\max(a_1 \omega, \Omega f_2)} \end{aligned}$$

and

$$\begin{aligned} \theta_x &= u \tau_{xx} + v \tau_{xy} + w \tau_{xz} + \mu^* \frac{\partial k}{\partial x} \\ \theta_y &= u \tau_{xy} + v \tau_{yy} + w \tau_{yz} + \mu^* \frac{\partial k}{\partial y} \\ \theta_z &= u \tau_{xz} + v \tau_{yz} + w \tau_{zz} + \mu^* \frac{\partial k}{\partial z} \\ \mu^* &= \mu_L + \sigma^* \mu_T \end{aligned}$$

where τ is the stress tensor. The source term is;

$$\mathbf{S} = \begin{pmatrix} 0 \\ 0 \\ 0 \\ 0 \\ 0 \\ \tau_{ij} \frac{\partial u_i}{\partial x_j} - \beta^* \rho \omega k \\ \frac{\gamma}{v_t} \tau_{ij} \frac{\partial u_i}{\partial x_j} - \beta \rho \omega^2 + 2\rho(1-f_1) \frac{1}{\omega} \frac{\partial k}{\partial x_j} \frac{\partial \omega}{\partial x_j} \end{pmatrix} \quad (5)$$

In the above equations, f_1 and f_2 are the blending functions. The parameters σ_k , σ_ω , β , β^* , and γ are closure coefficients for the turbulence model. The equations are discretized in space by a structured hexahedral grid using a cell centered finite-volume method. Since within the code each block is considered as a single entity, only flow and turbulence quantities at the block boundaries need to be exchanged. The governing equations are solved explicitly in a coupled manner through a five-stage Runge-Kutta scheme towards the steady state with local time stepping, residual smoothing and multigrid for convergence acceleration. In addition, a low speed preconditioner¹² is employed to simulate low ambient Mach number of the nozzle and jet plume flows. Further details of the numerical method can be found in Ref. 13.

B. Computational Model and Grid

The dual-stream BPR=2.7 (B27) nozzle model was used for this computational study. The fan exit diameter was $D_f = 28.1$ mm, and the fan exit height was 1.8 mm. The B27 nozzle configuration and radial coordinates are shown in Fig. 3. Jet plume deflection is achieved by the use of internal airfoil-shaped vanes. The vane configuration used consist of both single and double pairs of vanes with three different airfoil cross sections; NACA 0012, NACA 4412 and NACA 7514. The configurations were placed at various azimuth angles and angles of attack. For all cases simulated the vane chord length was 3 mm and the vane trailing edge was situated 2 mm upstream of the nozzle exit. The details of the simulated configurations are shown in Table 1.

Multi-block grids were generated for each vane configuration. As all the configurations are symmetric, only one half of the models were modeled to save computational expense. In order to simulate the jet flow, the grid extended about $3.8D_f$ radially outward from the nozzle centerline and over $20D_f$ downstream of the nozzle. The C-grid was used around each vane in the region near the exit plane to capture the features of boundary layer and wake flows accurately. The outer region grid for both cases are identical to simplify grid generation work. The patch-connection interpolation technical was then used to transfer flow variable information between non-matched connection surfaces. Fig. 4 shows the whole vane nozzle grid and the grid around vane.

C. Flow and Boundary Conditions

The experimental tests were performed with static free-stream conditions. Details of engine cycle analysis and resultant operating conditions of the B27 nozzle can be found in Ref. 2 and are summarized in Table 2. The “hot” condition matches the conditions determined by the engine cycle analysis and was used in the acoustic tests while the “cold” condition is that which was used in the mean velocity tests. In order to validate the computational simulations the cold condition was used for the initial simulations while the hot condition was used for the turbulence data. For the cold case the total temperature of both streams is set to ambient value. For numerical stability, in this work all cases were run with free-stream velocity at 17 m/s ($M_\infty=0.05$). The flow conditions imposed at the various boundaries were the same for both cases.

For the fan and core duct flows uniform total pressure was specified at the inlet surface corresponding to a perfectly expanded exit Mach number. For the ambient region surrounding the nozzle flow, a characteristic boundary condition was defined, and the downstream static pressure was set to the ambient pressure. All nozzle and vane solid walls were specified using the adiabatic no-slip boundary condition. The jet Reynolds number for the hot and cold conditions were 0.92×10^6 and 0.47×10^6 respectively based on fan nozzle exit diameter.

III. Experimental Details

The hot jet conditions are based on a cycle analysis for a supersonic turbofan engine presented in an earlier study². The bypass ratio is BPR=2.7, fan pressure ratio is FPR=2.2, and primary exhaust velocity is 600 m/s. As mentioned above the goal of implementing the fan flow deflectors is to reduce the jet noise emitted by the engines in the downward and sideline directions which were quantified by taking acoustics measurements, the details of which can be found in a previous study². Each acoustic test was followed by a mean velocity survey in a duplicate dual-stream apparatus. In the acoustic tests, helium-air mixtures are used to simulate the hot jet conditions, however for the mean velocity testing pure air was used for both primary and secondary streams due to the large run times of these tests. As pure air was used instead of helium-air mixtures the flow velocities were lower in the mean velocity tests than those from the engine cycle analysis and in the acoustic tests. However, the velocity ratio and primary Mach number were held the same as in the acoustic tests, as shown in Table 2.

The mean axial velocity in the jet plume was surveyed using a Pitot rake system consisting of five Pitot probes with hypodermic 0.5 mm internal diameter tips attached to a three dimensional traverse system, shown in Fig. 5. The very small diameter of the probe tips allowed a fine resolution of the velocity data, which facilitated the study of the subtle inflectional layers in the jet plume. The Pitot pressure was converted to velocity under the assumption of constant static pressure (equal to the ambient value) and constant total temperature (equal to room temperature). Smoothing of the velocity profiles, and computation of the velocity gradients, was performed using a Savitzky-Golay filter.

For each axial station, the radial derivatives were calculated on the radial-azimuthal ($r - \phi$) coordinate system (Fig. 6). The origin of the ($r - \phi$) system is defined as the centroid of the region where the Pitot pressure exceeds 95% of its maximum value. The first and second derivatives were calculated along radial lines from $\phi = 0$ to 358° in increments of 2° . The resulting radial velocity gradient is normalized in the form

$$G(x, r, \phi) = \frac{D_f}{U_p} \frac{\partial u(x, r, \phi)}{\partial r} \quad (6)$$

Inflection layers are extracted from the second radial derivative data (Fig. 6) and are defined by

$$i_{1,2,3}(x, \phi) = r(x, \phi) : \frac{\partial u^2(x, r, \phi)}{\partial r^2} = 0 \quad (7)$$

The primary core is defined as the region where the velocity exceeds 90% of the primary perfectly expanded velocity U_p .

Noise measurements were conducted inside an anechoic chamber and utilized an array of eight condenser microphones (Bruel & Kjaer, Model 4138) arranged on a circular arc centered at the vicinity of the nozzle exit. The polar aperture of the array is 30° and the array radius is 1 m. The angular spacing of the microphones was logarithmic. The entire array structure was rotated around its center to place the array at the desired polar angle. Further details on the acoustical measurement and noise source location procedure can be found in Ref. 2.

IV. Validation of the Computational Code

Computations and experiments tests were performed on various fan flow deflection configurations to provide insight into the physics of noise suppression. The configurations are presented in Table 1. The computational code is validated by comparing plots of the jet velocity, radial velocity gradients and plume inflection layers. The velocity plots presented consist of a comparison between velocity contour plots along the vertical symmetry plane, transverse velocity contour plots at various axial locations downstream of the jet exit and velocity line plots along the vertical symmetry plane at various axial locations. The gradient plots compare contours of radial velocity gradient along the vertical symmetry plane. Also presented are comparison plots of inflection layers highlighting the generalized secondary core along the vertical symmetry plane.

The results for the baseline nozzle are shown in Figs. 7–9. The velocity plots (Fig. 7) indicate excellent agreement between the experimental results and the computational simulation. The length of the potential cores are very similar at approximately $x/D_f=6$ however the computation is able to resolve the wake from the plug in finer detail than the experiments, possibly due to the finite diameter of the probe tip and the smoothing routines used. The growth rate of the computational and experimental jets are also very similar, as evidenced in the transverse contour plots and the overlapping of the velocity line plots. The radial velocity plots (Fig. 8) also display a high level of similarity, however, as with the velocity plots, the computational data displays a higher degree of detail close to the jet exit. Despite this, the overall shape and magnitude of the radial velocity gradients in the mid to far field agree very well. The length and shape of the generalized secondary cores in the inflectional layer plots (Fig. 9), shown as the green shaded regions, are also in excellent agreement. There is a small difference in the primary inflection layer in the vicinity of $x/D_f=6$ where the CFD predicts a “thinner” primary inflection layer than the experiments. This is also evidenced in the velocity line plots in Fig. 7, which show the computational line plots that are slightly thinner and more “peaky” than the experimental plots.

Velocity, radial velocity gradient and inflection layer data for the 4Va nozzle configuration with fan flow deflectors implemented are shown in Figs. 10–12. The data presented are representative of the data for all the fan flow deflection configurations that were studied. As with the baseline case, the velocity contour and line plots (Fig. 10) are all in very good agreement. The potential core lengths are slightly different, evidenced in the velocity contour plot along the vertical symmetry plane with the experimental data showing a slightly shorter potential core than the computation. Despite this the deflection of the jet is very similar. Particularly notable is the similarity in shape of the computational and experimental transverse velocity contour plots. The velocity line plots close to the jet exit also show excellent agreement in resolving the deflected secondary stream on the underside of the jet. The radial velocity gradient contour plots (Fig. 11) for this configuration are in general agreement with some small discrepancies. Consistent between the computation and experiment is the increase in gradient magnitude on the top of the jet and the general decrease in velocity gradient on the underside of the jet. This is significant, as previous experiments have shown a significant correlation between reduction in velocity gradients and directional noise suppression from asymmetric dual-stream jets. While the general shape and magnitude of the contours are similar the computation indicates a much higher gradient between the primary and secondary stream on the underside of the jet. The experiment also indicates slightly lower velocity gradients on the underside of the jet than the computation. Excellent agreement is achieved in this case between the inflectional layer plots of the experiment and computation (Fig. 12). The lengths of the generalized secondary cores on the top and underside of the jet are equal and the shapes of the primary inflection layers are very comparable.

Using the above plots as a qualitative metric together with quantitative measurements of the potential and generalized secondary core lengths and deflection levels, in conjunction with the other cases studied, a high level of confidence can be inferred for the use of the computational code to effectively simulate the flow and capture the important features of the actual jet plume. Thus it is possible to use this code to obtain flow quantities such as turbulent kinetic energy that cannot be measured directly with the current facilities available.

V. Temperature Effects

The mean velocity experiments from which the computational code was validated were performed using “cold” conditions that matched the velocity ratio and primary Mach number of the “hot” conditions. The acoustic experiments were performed using helium – air mixtures to simulate the hot jet exit conditions that were found from a previous engine cycle analysis study. Thus it is necessary to investigate the effect of temperature, which changes the jet exit conditions, to obtain an accurate representation of the jet using the computational code.

Presented in this section are two configurations, the baseline and a 4-vane configuration with NACA 7514 airfoil vanes (4Va), which highlight the similarities and differences between the jets at the different flow conditions that are representative of the majority of flow deflected configurations. The comparison is made using composite mean velocity plots as in Section IV and contour plots of the normalized turbulent kinetic energy along the vertical symmetry plane and in the transverse direction at various axial locations downstream of the jet exit. The turbulent kinetic energy, k , was normalized in the form;

$$k^* = \frac{k}{U_p^2} \quad (8)$$

The temperature comparison results for the baseline configuration are presented in Figs. 13 – 15. The velocity contour plots and line plots (Fig. 13) show the growth rate of the hot jet is much greater than the jet operating at cold conditions. This increased growth rate, due to higher levels of mixing, also results in a shorter potential core for the hot jet compared to the cold. Despite the differences in growth rate, the two jets maintain similar velocity profiles, particularly close to the jet exit, in resolving the influence of the secondary plume and the wake from the plug.

The turbulent kinetic energy plots for the baseline nozzle in the vertical symmetry plane (Fig. 14) and in the transverse direction (Fig. 15) also highlight the increased growth rate of the hot jet compared to the cold jet. The contours of higher k extend downstream considerably more in the cold case than the hot and the location of peak k is further upstream and slightly lower in magnitude for the hot jet with a peak value of $k^*=0.0239$ for the cold jet and $k^*=0.0212$ for the hot jet. It is important to note that the location of the peak turbulent kinetic energy compared with the location of the end of the potential core is consistent between the hot jet and the cold jet. While the potential core is shorter when the jet is run at hot conditions the turbulent kinetic energy plots indicate that the influence of the secondary stream propagates further downstream than in the cold case.

Comparison plots for the 4Va configuration are shown in Fig. 16 – Fig. 18. The plots of the velocity contours and velocity profiles (Fig. 16) show similar trends to the baseline case with the hot jet having a significantly shorter potential core than the cold jet. The profile shapes are generally quite similar however the cold case seems to give a slightly higher downward distortion, evidenced in the transverse velocity contour plots.

The turbulent kinetic energy contour plots in Fig. 17 and Fig. 18 highlight the effect of the flow deflection on the different in turbulent kinetic energy that is generated on the top of the jet compared with the underside. As with the baseline case, the magnitude of k^* is generally higher in the far field of the cold jet compared to the hot jet. The magnitude of the peak k^* is again higher in the cold jet at $k^*=0.0274$ on top of the jet and $k^*=0.0153$ on the underside of the jet compared with $k^*=0.0258$ and $k^*=0.0119$ on the top and underside of the hot jet respectively. As with the baseline case the position of the peak turbulent kinetic energy with the respect to the end of the potential core is the same in the hot and cold jets. As with the baseline configuration the turbulent kinetic energy contour plots along the vertical symmetry plane indicate a greater influence and extent of the secondary plume, particularly on the underside of the jet in the deflected cases, for the jet at the hot cycle point compared with the cold case.

In the previous figures, the velocity profiles for the “cold” and “hot” conditions are compared at the same axial distance (normalized by fan diameter). Given that a major effect heating is reduction of the primary potential core length L_p , it is instructive to also compare profiles at the same x/L_p . Such comparisons are shown in Fig. 19 and Fig. 20 for the baseline nozzle and the 4Va configuration respectively. For the baseline nozzle (Fig. 19) the velocity profiles nearly collapse for the hot and cold cases when the axial location is non-dimensionalized by the respective primary core length of each jet plume. A reasonable collapse also occurs for the 4Va fan flow deflection configuration (Fig. 20). After accounting for the potential core length, Bridges also observed the collapse of velocity profiles for single stream jets with different temperatures¹⁵. When the axial distance was normalized using the potential core length of the jet, it was discovered that the velocity and mean squared velocity curves for the jets

of varying temperatures collapsed to a single curve. The potential core length that was used was determined theoretically using the Witze correlation parameter¹⁶, which takes into account variations in temperature and velocity for subsonic jets. In a subsequent study Bridges and Wernet additionally found that the spectral characteristics and space-time correlations of turbulence in the jet were temperature invariant after taking into account the potential core length¹⁷.

VI. Turbulent Kinetic Energy

The normalized turbulent kinetic energy contour plots for the baseline nozzle are shown in Fig. 21. The distribution of k^* is axisymmetric with a peak value of $k^*=0.0239$. The transverse contour plot close to the jet exit shows a small level of k^* between the primary and secondary cores and a larger level between the secondary core and the ambient. As noted previously the location of the peak turbulent kinetic energy occurs close to the merging of the shear layers in the intermediate region of the jet close to the end of the potential core. The azimuthal variation of k^* is shown in Fig. 22 with $\phi = 0^\circ$ corresponding to the downward direction and $\phi = 180^\circ$ corresponding to the upward direction. The plot confirms that there is no azimuthal variation in the turbulent kinetic energy and shows the peak k^* occurs at an axial distance of approximately $x/D_f = 4.0$.

A typical deflected case is presented in Fig. 23, showing the turbulent kinetic energy contours of a 4-vane configuration using NACA 4412 airfoil vanes (4Vd). The contour plots of k^* show the decrease in turbulent kinetic energy on the underside of the jet with a small increase in the turbulent kinetic energy on the top of the jet. The turbulent kinetic energy is decreased to $k^*=0.0142$ in the downward direction and $k^*=0.0160$ in the sideline direction equating to a 33% and 25% decrease respectively. The normalized turbulent kinetic energy increases to $k^*=0.0268$, a 26% increase over the baseline level. Again the peak turbulent kinetic energy is located close to the end of the potential core. From the transverse contour plots a general decrease in k^* is evident over the whole bottom region of the jet plume. This is demonstrated to more clearly in Fig. 22, which shows the absolute normalized turbulent kinetic energy contours over the azimuthal range (Fig. 24a) and the change in turbulent kinetic energy with respect to the baseline case (Fig. 24b). There is a general increase on the top of the jet with a peak from $\phi = 180^\circ$ to $\phi = 140^\circ$ and a decrease in turbulent kinetic energy on the underside of the jet. This decrease extends from $\phi = 0^\circ$ past the sideline direction to $\phi = 70^\circ$ and persists over a reasonably large axial range from $x/D_f = 2.2$ to $x/D_f = 6.0$ with a peak at approximately $x/D_f = 4.0$.

The peak turbulence data for all the cases computed is shown in Table 3 and shows values of k^* and percentage decrease or increase in the downward, sideline and upward directions. A notable trend evident in the table is that generally a decrease in k^* in the downward direction is accompanied by a corresponding increase in k^* in the upward direction, although typically less than the decrease. According empirical relation between noise level and turbulent kinetic energy³, a decrease in the magnitude of k^* indicates there will be significant noise suppression.

Due to the strong relationship between turbulent kinetic energy and the noise produced it is beneficial to investigate the correlation between the experimental noise measurements in the form of peak overall sound pressure level (OASPL) in the downward and sideline directions and the turbulent kinetic energy than was determined using the computations. The peak overall sound pressure level is determined from the noise spectrum in the polar direction of peak noise emission, Fig. 25a, for the baseline nozzle. The axial location of peak noise emission can be determined using the noise spectrum in the direction of peak emission, Fig. 25a, and a noise source map in the vicinity of the peak direction, Fig. 25b. The peak sound pressure level occurs at a frequency of approximately $f_{max} = 0.12$ kHz. The noise source map (Fig. 25b) can then be used to determine the axial location of the highest intensity at this frequency. For a frequency of $f_{max} = 0.12$ kHz the maximum intensity occurs at an axial location of $x/D_f = 5.5$. A correlation can then be made between the peak OASPL at $\phi = 0^\circ$ (downwards) and $\phi = 60^\circ$ (sideline) and the peak turbulent kinetic energy at $x/D_f = 5.6$ for the downward and sideline azimuth angles, shown in Fig. 26.

While the number of data points is limited at this point in time, the trend of noise reduction versus turbulent kinetic energy reduction is evident. The data presented in Fig. 26 shows that with increasing turbulent kinetic energy reduction there is an initial sharp increase in the noise reduction followed by an asymptotic flattening behavior as the reduction in turbulent kinetic energy becomes greater. As a larger number of computational cases for the hot jet are completed we anticipate this correlation to become more defined.

VII. Conclusions

A computational and experimental study was conducted for a dual-stream supersonic turbofan engine with several fan flow deflector configurations. The aim of the investigation was to validate a computational model of the jet flow with experimental results, determine the effects of hot and cold operating conditions on the jet velocity profile and turbulent kinetic energy, study the turbulent kinetic energy effects of different fan flow deflection

configurations and investigate the connection between noise reduction and the turbulent kinetic energy in the jet plume in various propagation directions.

The computational validation was performed by comparing mean velocity fields, radial velocity gradient fields and inflectional layer plots found using CFD with those determined experimentally for the baseline nozzle and several nozzles with various fan flow deflector configurations implemented. The computational results agreed very well with the experimental results for all cases, however close to the jet exit the computational model generally showed more detail than the experimental results, possibly due to the finite resolution of the Pitot probes.

The comparison of hot and cold jets indicated, as expected, that the hot jet has higher levels of mixing giving a larger growth rate and shorter potential core. The computations also indicated that over the entire jet plume the turbulent kinetic energy in the hot jet was lower than the cold jet. When the axial distance was non-dimensionalized by the potential core lengths of the hot and cold jets respectively the velocity profiles almost collapsed on the same curve, indicating the physical elements of the jet are reasonably consistent regardless of the temperature.

The turbulent kinetic energy results for the fan flow deflection configurations determined using CFD showed a general decrease in k on the underside of the jet and a corresponding increase in k on top of the jet. It is notable that the location of peak turbulent kinetic energy occurs close to the end of the potential core for all cases studied.

A preliminary correlation was established between the peak overall sound pressure level (OASPL) and the turbulent kinetic energy in the jet plume. The correlation results indicate a hyperbolic tangent-like trend that suggests a rapid increase in noise reduction for small reductions of k with slower noise decreases as k increases. This trend matches those found between noise and velocity gradient decreases and inflectional layer volume in previous studies^{6,14}.

This study provides a solid framework for the continuing investigation of noise reduction in supersonic turbofan engines implemented with fan flow deflectors. Using this computational code it will be possible to determine aerodynamic properties of the deflectors and the corresponding mass and thrust loss that results from their implementation. Additionally it will be possible to perform an airfoil optimization scheme to determine the optimal airfoil shape and placement to achieve the highest noise reduction for low thrust loss.

Acknowledgements

The support by NASA Cooperative Agreement NNX07AC62A (monitored by Dr. K.B.M.Q. Zaman) is gratefully acknowledged. We thank Mr. Vincent Phong for his assistance with the design and fabrication of the vanes.

References

- ¹Papamoschou, D., "Fan Flow Deflection in Simulated Turbofan Exhaust," *AIAA Journal*, Vol. 44, No.12, 2006, pp. 3088-3097.
- ²Papamoschou, D., and Nielsen, P., "Fan Flow Deflection for Supersonic Turbofan Engines," *AIAA Paper* 2008-0039, Jan. 2008.
- ³Birch, S.F., Lyubimov, D.A., Maslov, V.P., and Secundov, A.N., "Noise Prediction for Chevron Nozzle Flows," *AIAA Paper* 2006-2600, May 2006.
- ⁴Shupe, R.S., Zaman, K.B.M.Q., and Papamoschou, D., "Effect of Wedge-Shaped Deflectors on Flow Fields of Dual-Stream Jets," *AIAA Paper* 2007-3659, May 2007.
- ⁵Dippold, V., Foster, L., and Wiese, M., "Computational Analyses of Offset Stream Nozzles," *AIAA Paper* 2007-3589, May 2007.
- ⁶Nielsen, P., and Papamoschou, D., "Optimization of Fan Flow Deflection for Supersonic Turbofan Engines," *AIAA Paper* 2008-3061, May 2008.
- ⁷Jameson, A., Schmift W., and Turkel, E., "Numerical solutions of the Euler Equations by Finite Volume Methods Using Runge-Kutta Time Stepping Scheme," *AIAA Paper* 1981-1259, Jan. 1981.
- ⁸Bladwin, B.S., Lomax, H., "Thin-Layer Approximation and Algebraic Model for Separation Flows," *AIAA Paper* 1978-257, 1978
- ⁹Spalart, P.R. and Allmaras, S.R., "A One-Equation Turbulence Model for Aerodynamic Flows," *AIAA Paper* 1992-0439, Jan. 1992.
- ¹⁰Wilcox, D.C., "Reassessment of the Scale Determining Equation for Advanced Turbulence Models", *AIAA Journal*, Vol. 26, No. 11, 1988, pp. 1299-1310.
- ¹¹Menter, F.R., "Two-Equation Eddy-Viscosity Turbulence Models for Engineering Applications," *AIAA Journal*, Vol. 32, No.8, 1994, pp. 1598-1605.
- ¹²Turkel, E., "A Review of Preconditioning Methods for Fluid Dynamics," *Applied Numerical Mathematics*, Vol. 12, No.1 1993, pp. 257-284
- ¹³Liu, F. and Zheng, X., "A Strongly Coupled Time-Marching Method for Solving the Navier-Stokes and $k-\omega$ Turbulence Model Equations with Multigrid," *Journal of Computational Physics*, Vol. 128, No. 10, 1996.

¹⁴Nielsen, P., and Papamoschou, D., “Mean Flow – Acoustic Correlations for Dual-Stream Asymmetric Jets,” *AIAA Paper* 2009-0853, Jan. 2009.

¹⁵Bridges, J., “Effect of Heat on Space-Time Correlations in Jets,” *AIAA Paper* 2006-2534, May 2006.

¹⁶Witze, P.O., “Centerline Velocity Decay of Compressible Free Jets,” *AIAA Journal*, Vol. 12, No. 4, 1974, pp. 417-418.

¹⁷Bridges, J., and Wernet, M., “Effect of Temperature on Jet Velocity Spectra,” *AIAA Paper* 2007-3628, May 2007.

Table 1. Details of the fan flow deflector configurations used in computational and experimental tests.

Configuration	Airfoil	c [mm]	x_{TE} [mm]	α_1 [deg]	ϕ_1 [deg]	α_2 [deg]	ϕ_2 [deg]
Baseline	-	-	-	-	-	-	-
2V	0012	3.0	-2.0	7.5	90	-	-
4Va	7514	3.0	-2.0	4.0	50	4.0	120
4Vb	0012	3.0	-2.0	7.5	50	7.5	120
4Vc	0012	3.0	-2.0	7.5	90	7.5	150
4Vd	4412	3.0	-2.0	7.5	90	4.0	150

Table 2. Exhaust conditions for the B27 nozzle used in computational and experimental tests.

		Hot (cycle point)	Cold
Primary	U_p [m/s]	600	319
	M_p	1.03	1.03
	NPR_p	2.00	1.96
Secondary	U_s [m/s]	400	213
	M_s	1.15	0.65
	NPR_s	2.25	1.33
A_s/A_p		1.40	1.40
U_s/U_p		0.67	0.67

Table 3. Peak turbulent kinetic energy data in the downward, sideline and upward directions.

Configuration	$\phi = 0^\circ$ (down)		$\phi = 60^\circ$ (side)		$\phi = 180^\circ$ (up)	
	k/U_p	Percent change	k/U_p	Percent change	k/U_p	Percent change
Baseline	0.0212	0%	0.0212	0%	0.0212	0%
2V	0.0155	-27%	0.0170	-20%	0.0235	+11%
4Va	0.0119	-43%	0.0194	-8%	0.0258	+22%
4Vb	0.0145	-32%	0.0190	-10%	0.0254	+20%
4Vc	0.0157	-26%	0.0168	-21%	0.0264	+25%
4Vd	0.0142	-33%	0.0160	-25%	0.0268	+26%

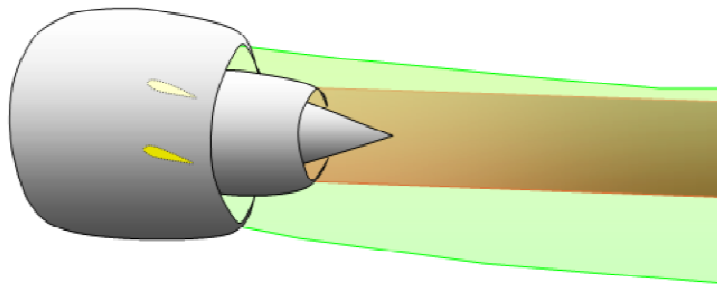
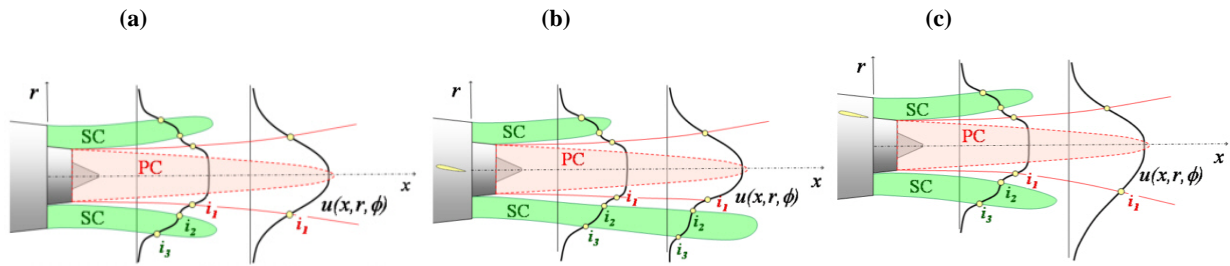


Fig. 1 General concept of fan flow deflection.



i_1, i_2, i_3 =inflection points of radial velocity profile; PC=primary core, defined by a velocity threshold (e.g., $u/U_p \geq 0.8$); SC=secondary core, defined by the loop of inflection points i_2 and i_3

Fig. 2 Possible deformations of velocity profile, from the coaxial state (a), by the action of fan flow deflectors: (b) Elongation of secondary core; (c) reduction in the downward velocity gradient.

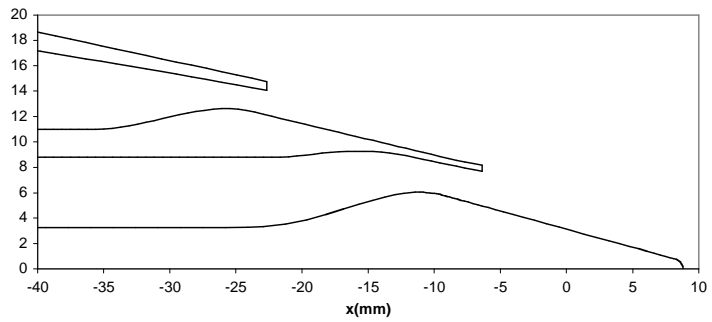
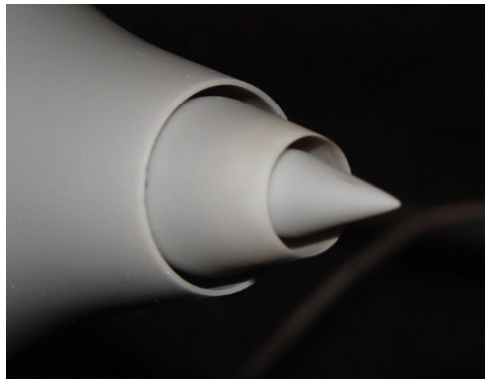
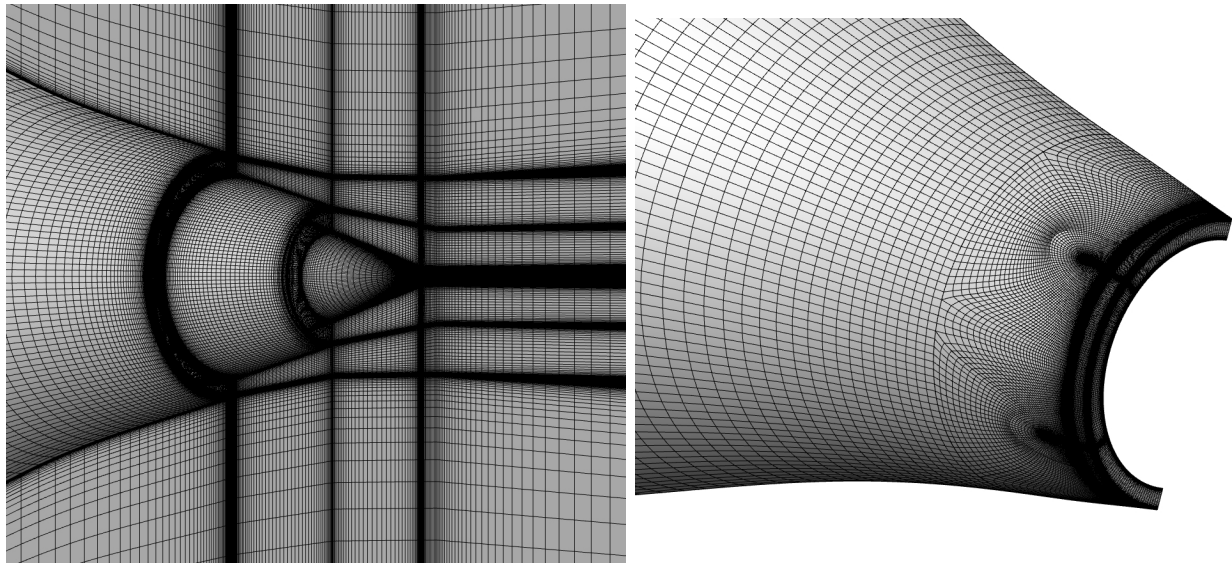


Fig. 3 Assembled nozzle and coordinates of the bypass ratio BPR = 2.7 (B27) nozzle.



(a)

(b)

Fig. 4 Computational grid of baseline nozzle (a) and detail of the grid around the vanes for the secondary nozzle flow (b).

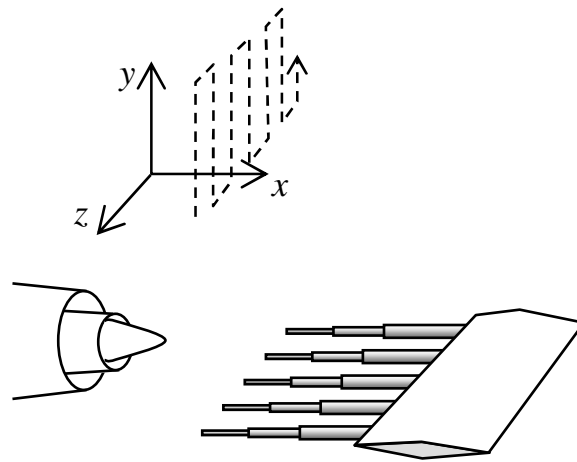


Fig. 5 Illustration of hypodermic tip Pitot rake with nozzle and traverse path.

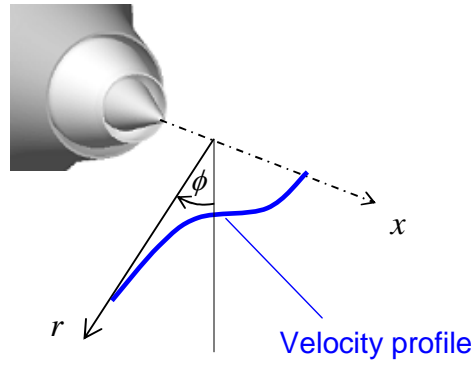


Fig. 6 Illustration of radial-azimuth coordinate system for computation of radial derivatives.

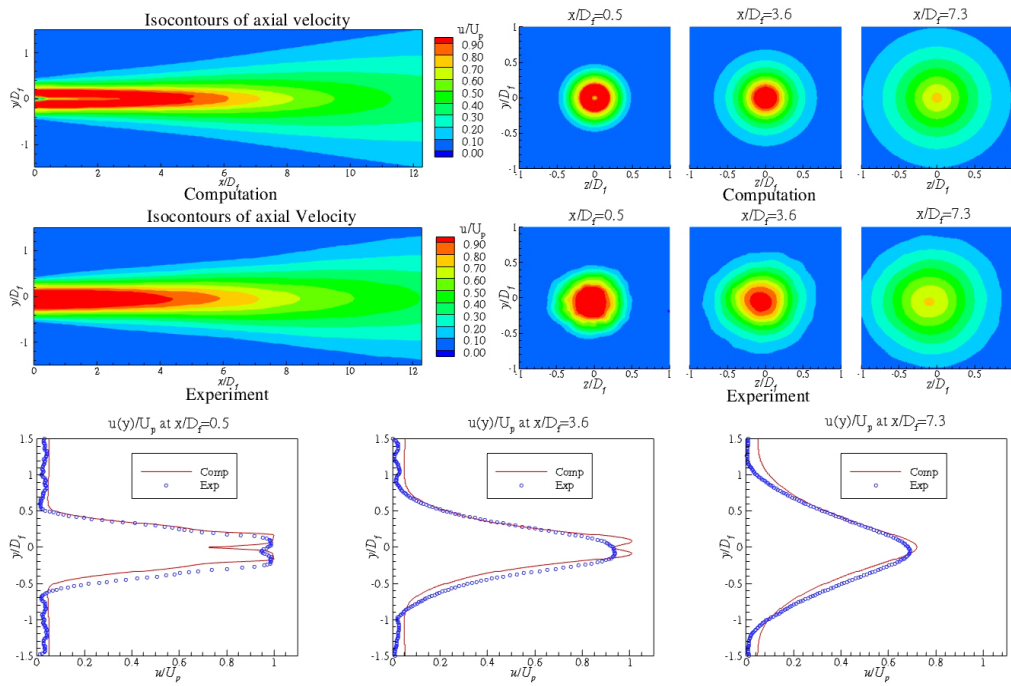


Fig. 7 Comparison of computational and experimental velocity field for the baseline nozzle.

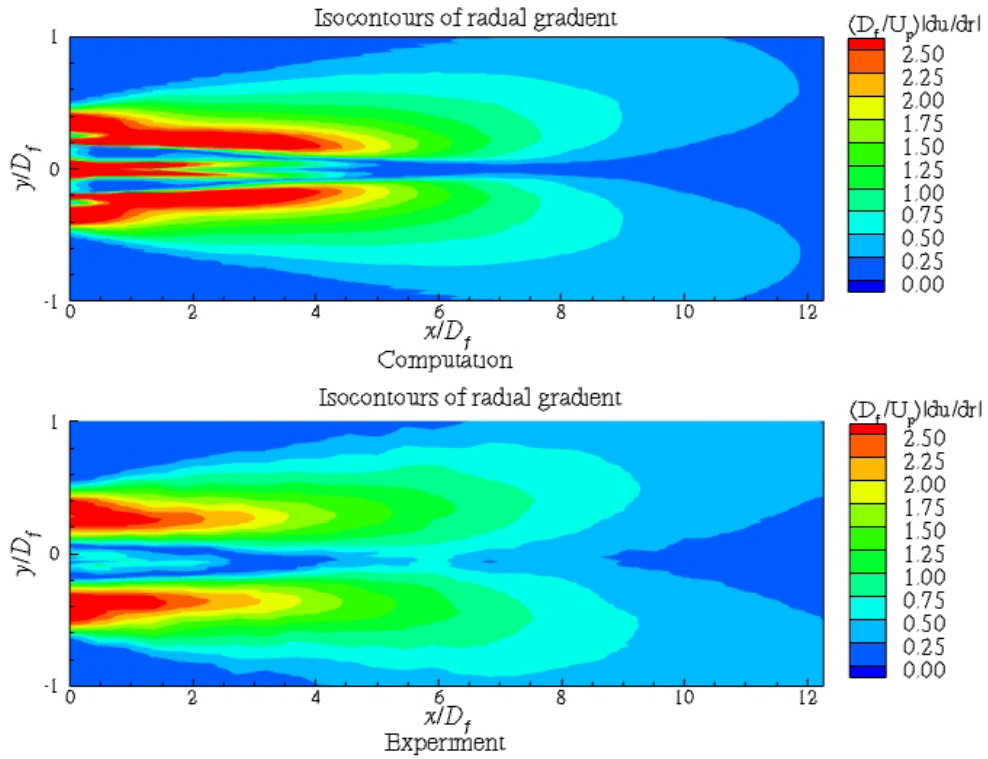


Fig. 8 Comparison of computational and experimental radial velocity gradient field for the baseline nozzle.

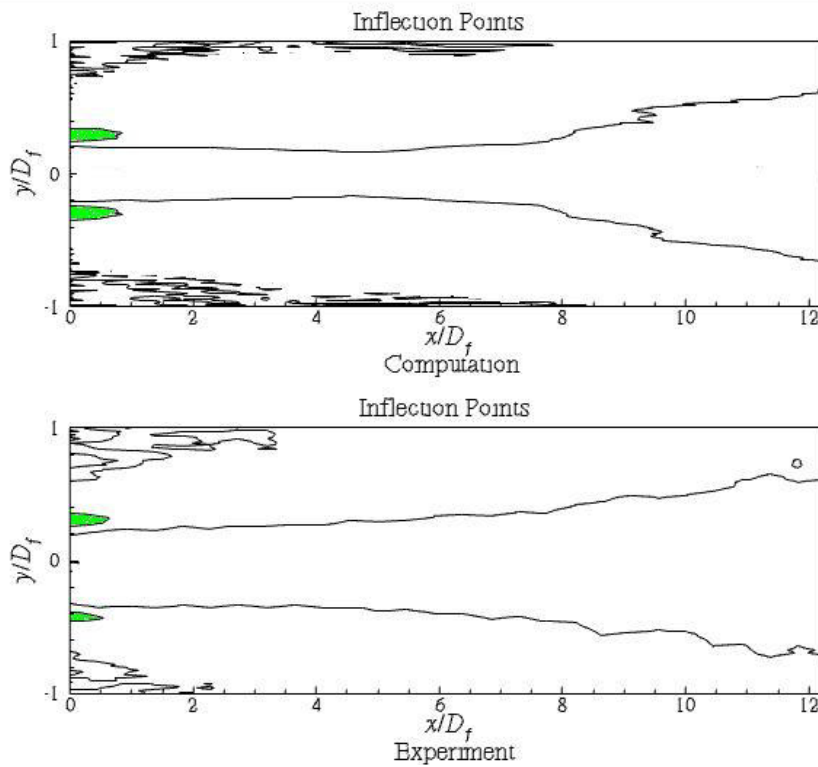


Fig. 9 Comparison of computational and experimental inflectional layers for the baseline nozzle.

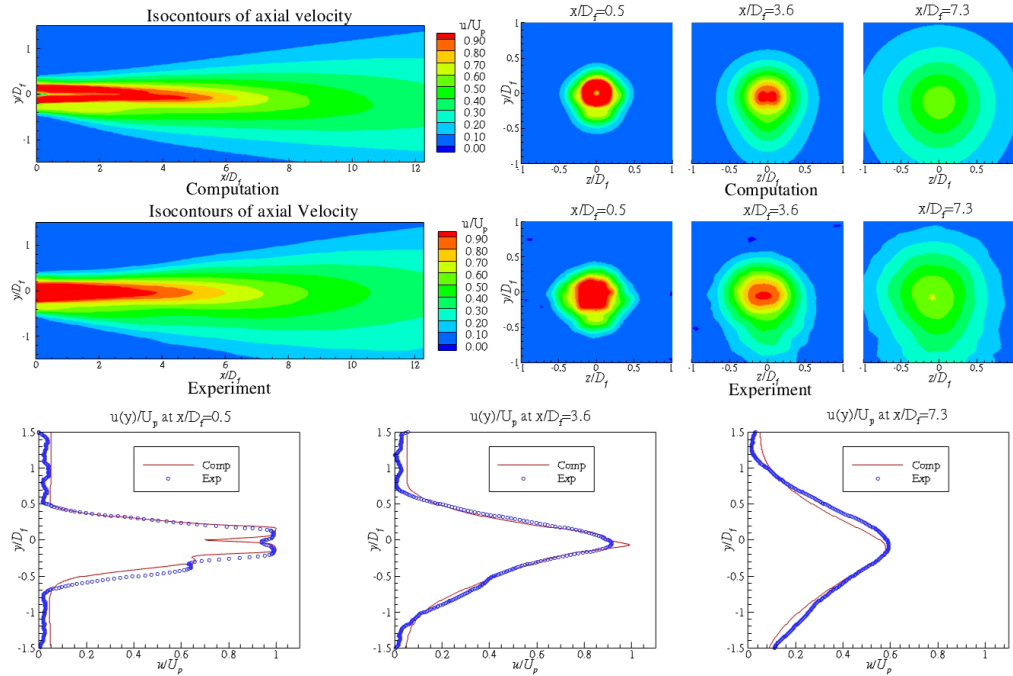


Fig. 10 Comparison of computational and experimental velocity field for the 4Va configuration.

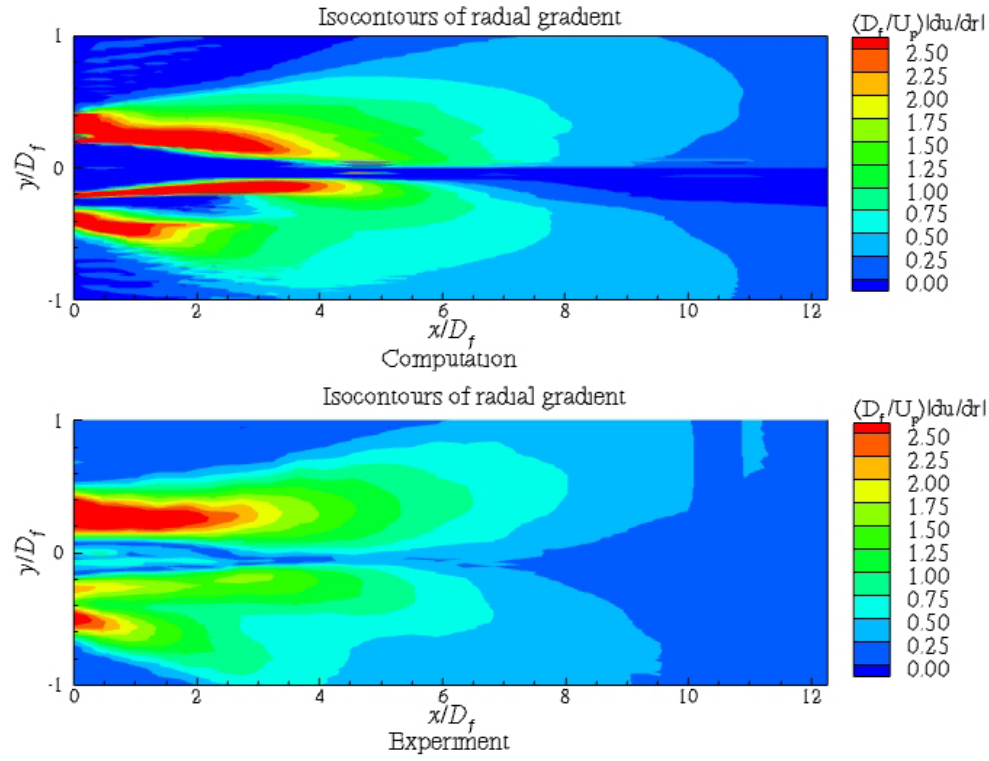


Fig. 11 Comparison of computational and experimental radial velocity gradient field for the 4Va configuration.

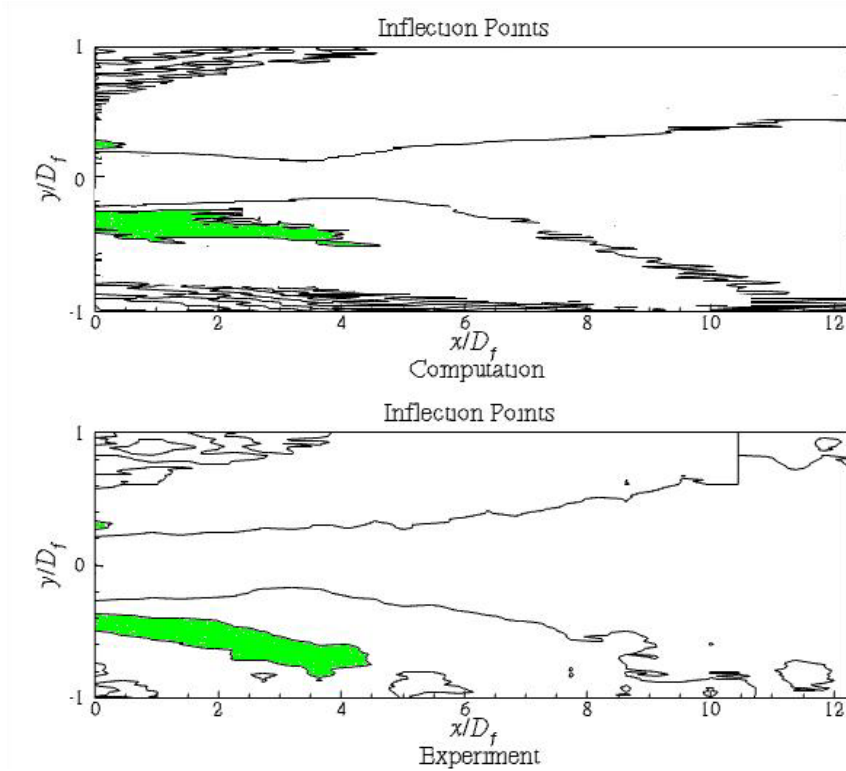


Fig. 12 Comparison of computational and experimental inflectional layers for the 4Va configuration.

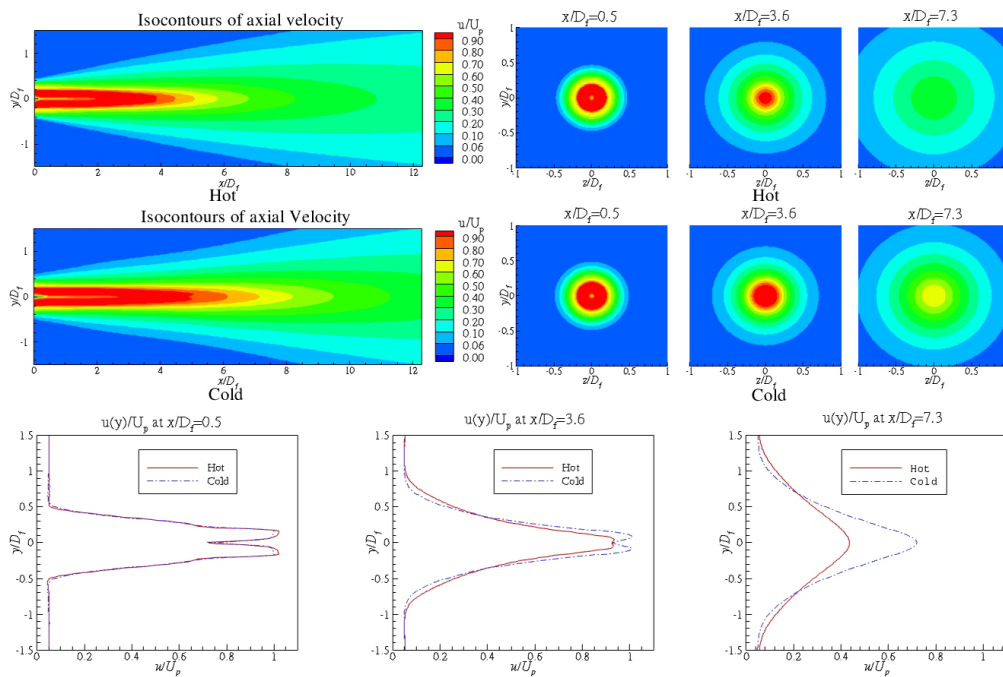


Fig. 13 Comparison of velocity profiles for hot and cold operating conditions for the baseline nozzle.

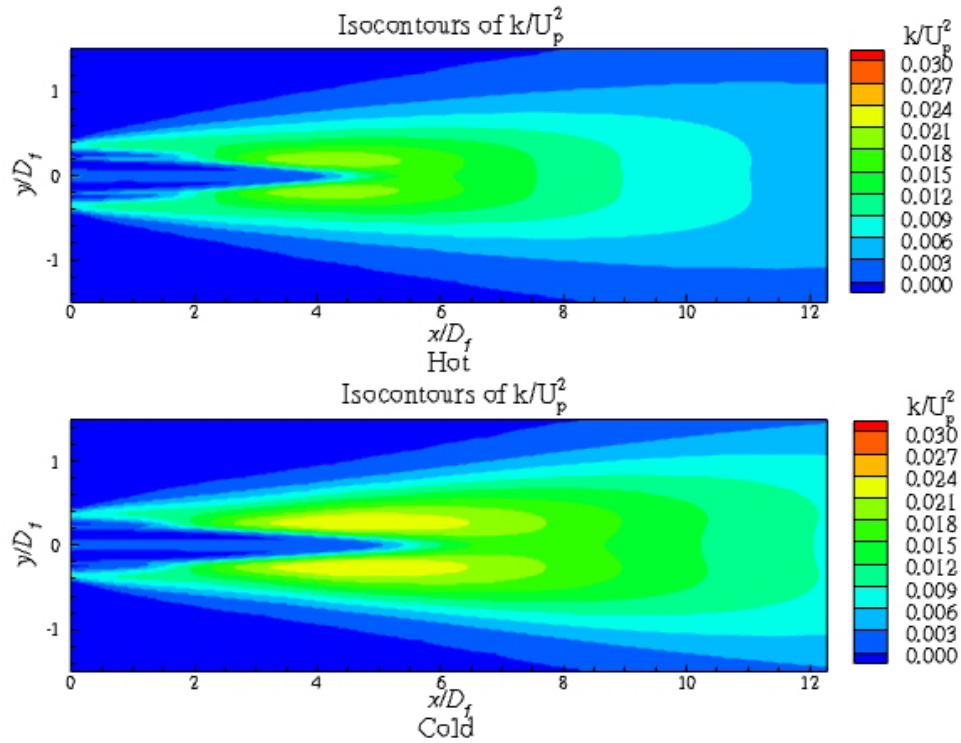


Fig. 14 Comparison of turbulent kinetic energy along the vertical symmetry plane for hot and cold operating conditions for the baseline nozzle.

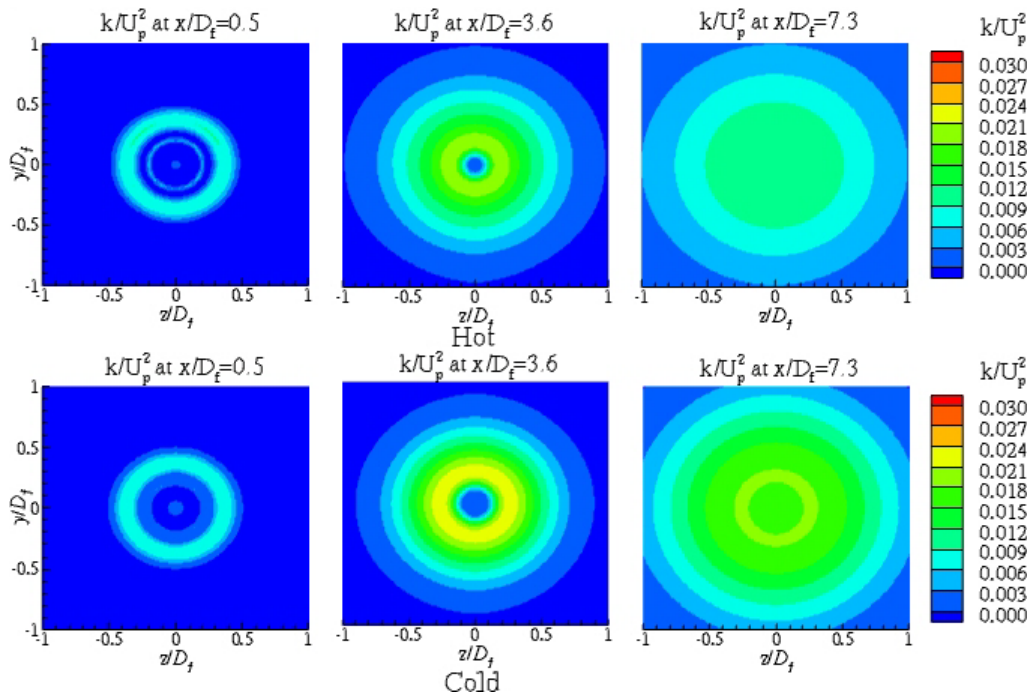


Fig. 15 Comparison of turbulent kinetic energy on the transverse plane at various axial distances for hot and cold operating conditions for the baseline nozzle.

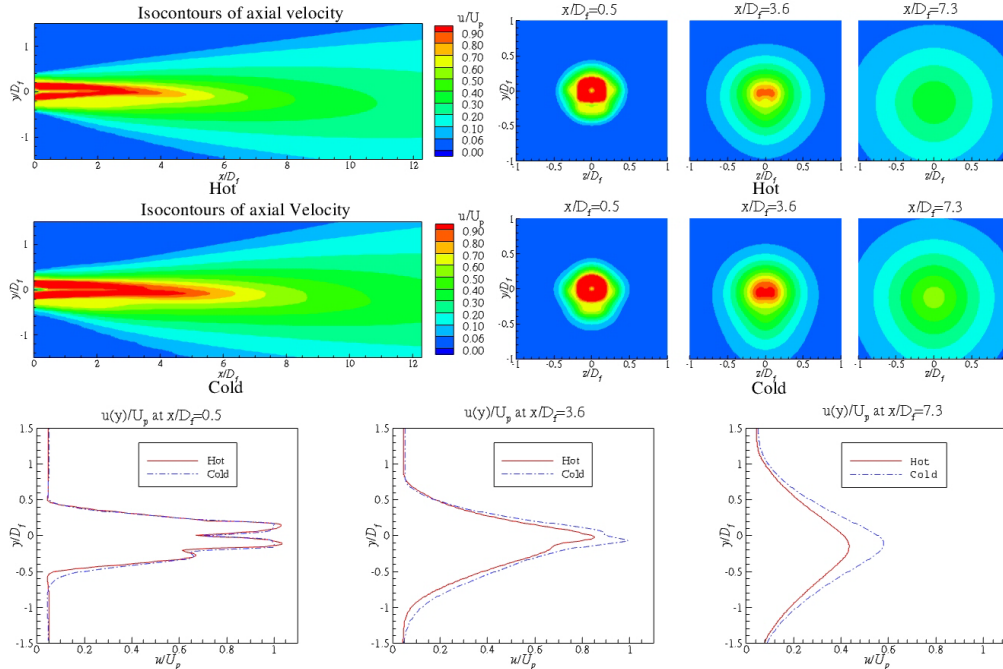


Fig. 16 Comparison of velocity profiles for hot and cold operating conditions for the 4Va configuration.

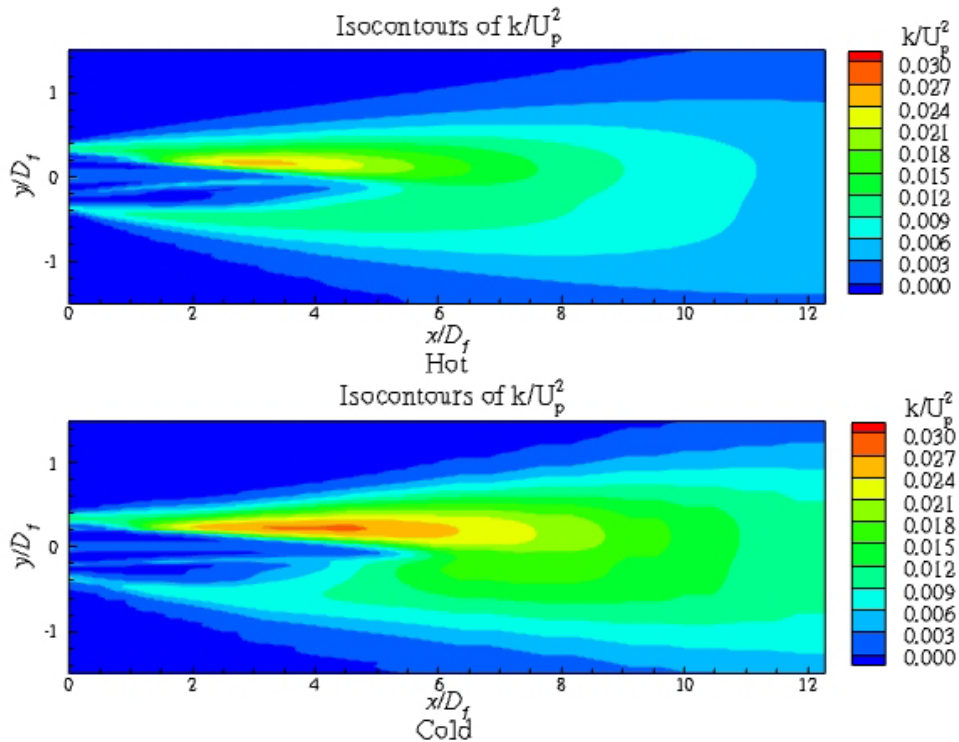


Fig. 17 Comparison of turbulent kinetic energy along the vertical symmetry plane for hot and cold operating conditions for the 4Va configuration.

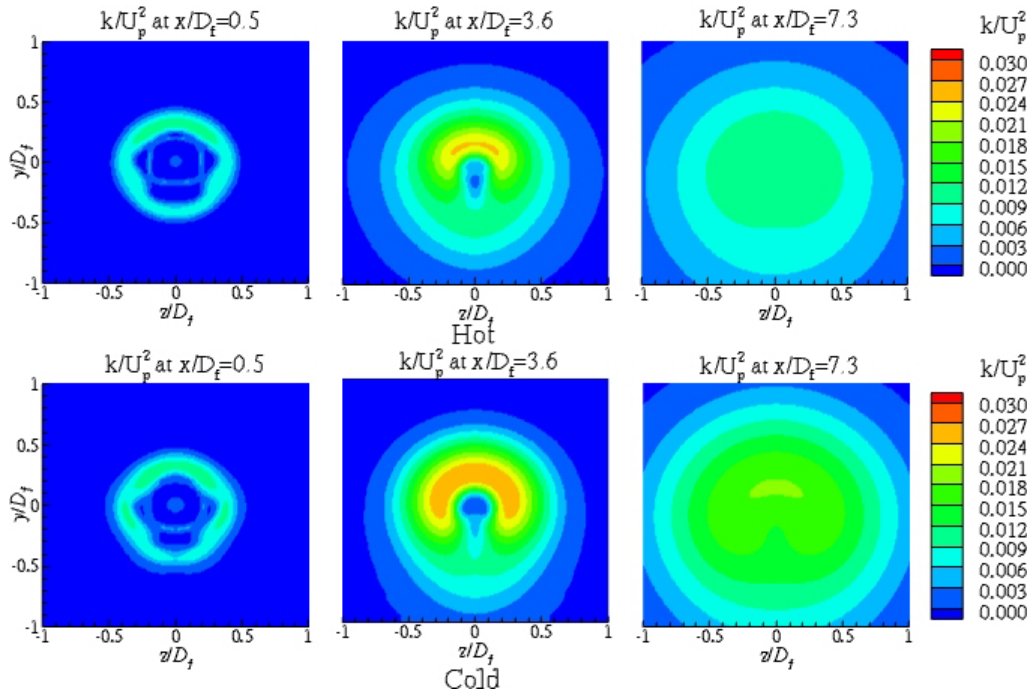


Fig. 18 Comparison of turbulent kinetic energy on the transverse plane at various axial distances for hot and cold operating conditions for the 4Va configuration.

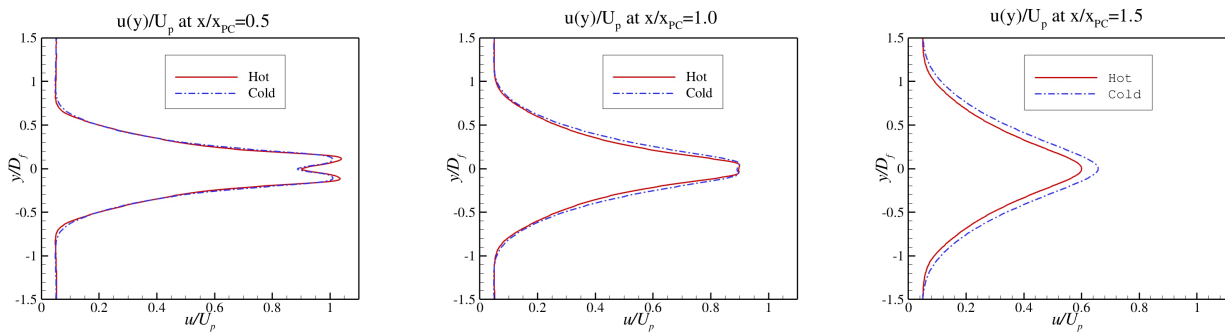


Fig. 19 Comparison of baseline nozzle velocity profiles at various axial distances that have been non-dimensionalized by the potential core lengths of the hot and cold jets respectively.

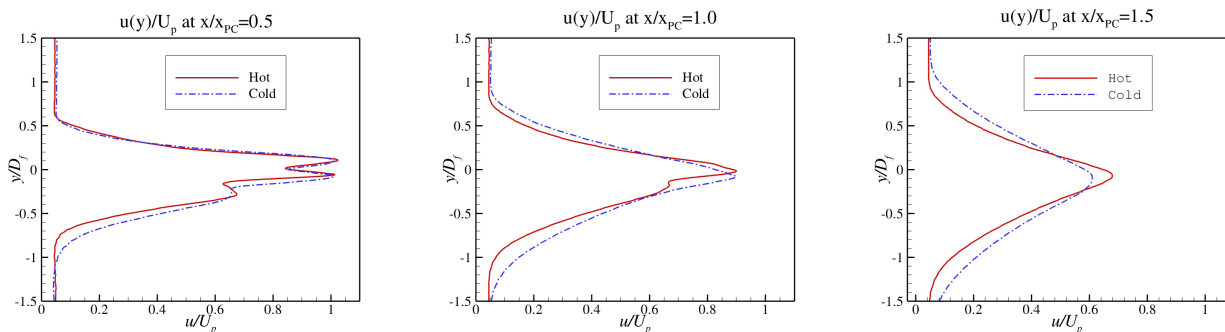


Fig. 20 Comparison of 4Va configuration velocity profiles at various axial distances that have been non-dimensionalized by the potential core lengths of the hot and cold jets respectively.

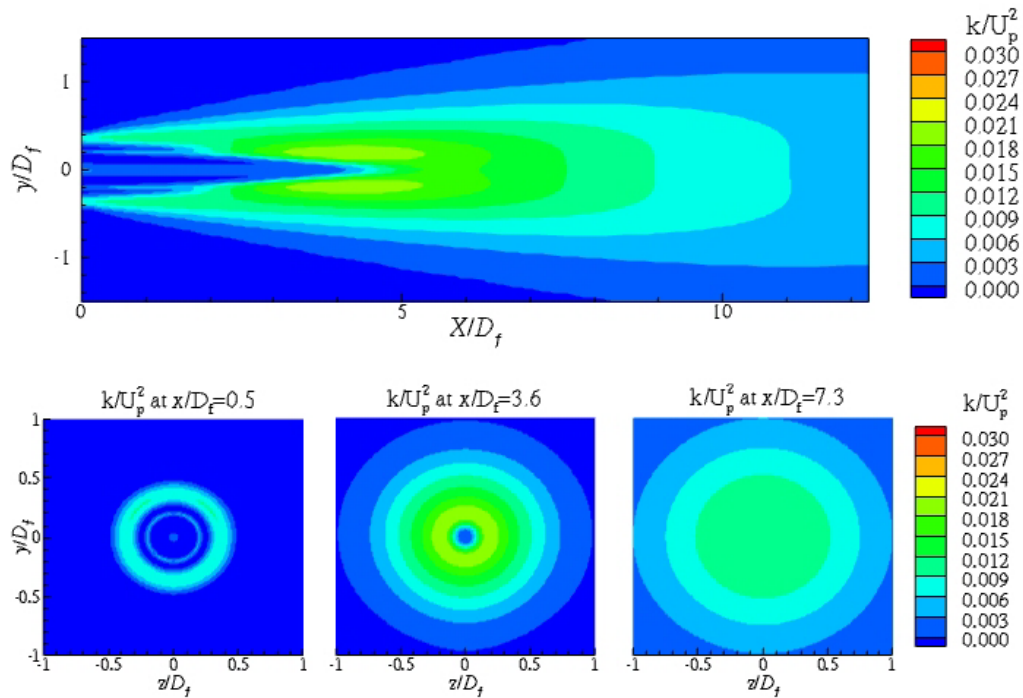


Fig. 21 Turbulent kinetic energy field for the baseline nozzle at hot operating conditions.

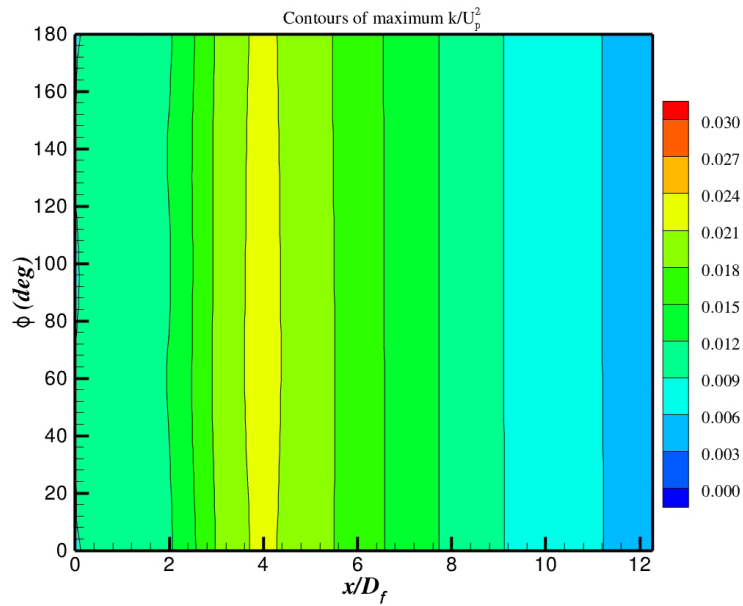


Fig. 22 Azimuthal variation of turbulent kinetic energy for the baseline nozzle at hot operating conditions.

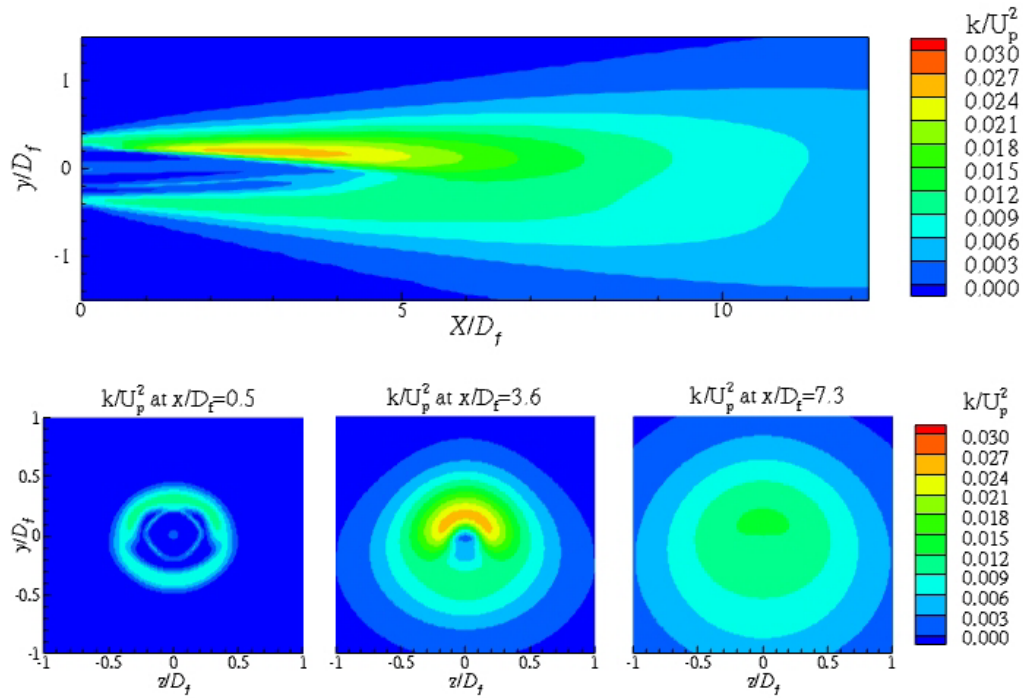


Fig. 23 Turbulent kinetic energy field for the 4Vd configuration at hot operating conditions.

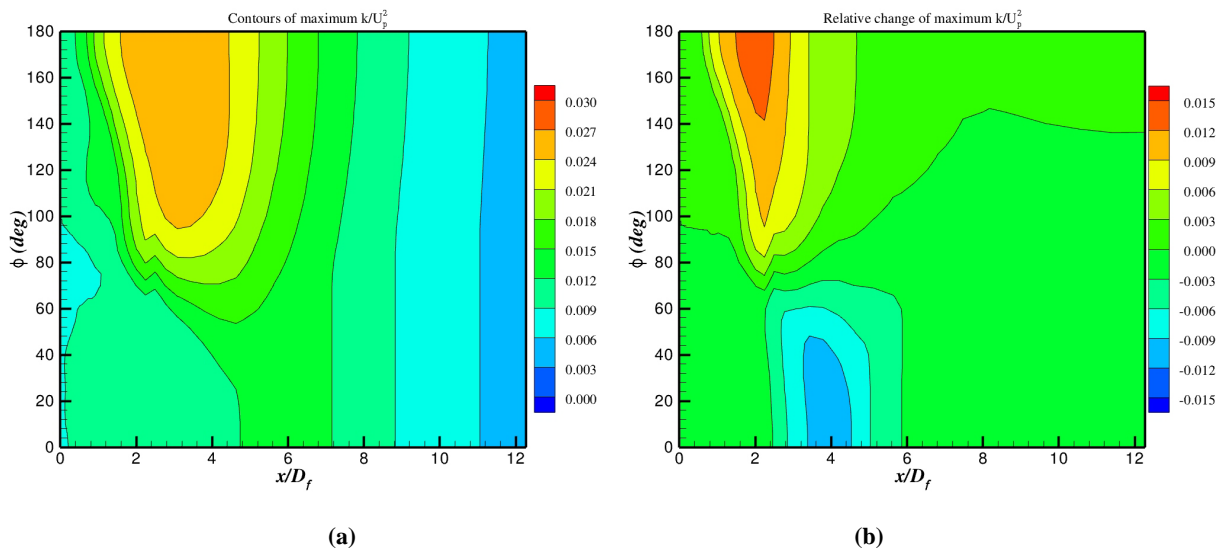


Fig. 24 Azimuthal variation of turbulent kinetic energy (a) and azimuthal variation with respect to the baseline nozzle (b) for the 4Vd configuration at hot operating conditions.

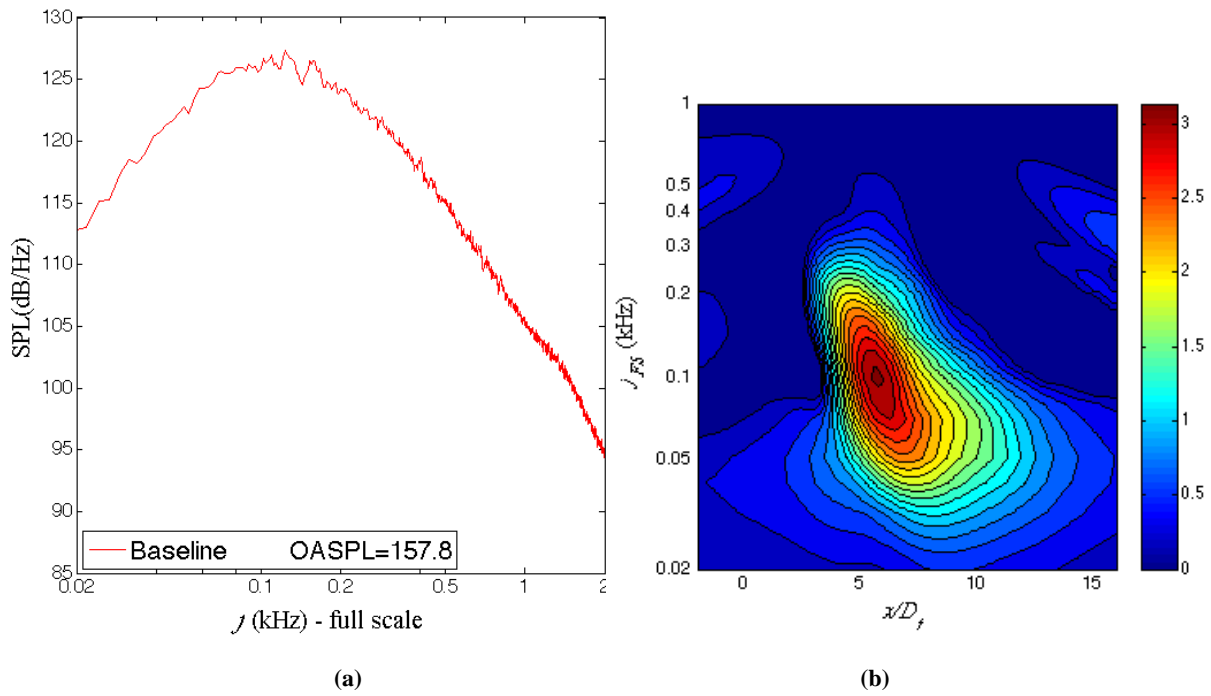


Fig. 25 Sound pressure level spectrum in the direction of peak OASPL (a) and noise source map in the direction of peak noise emission (b).

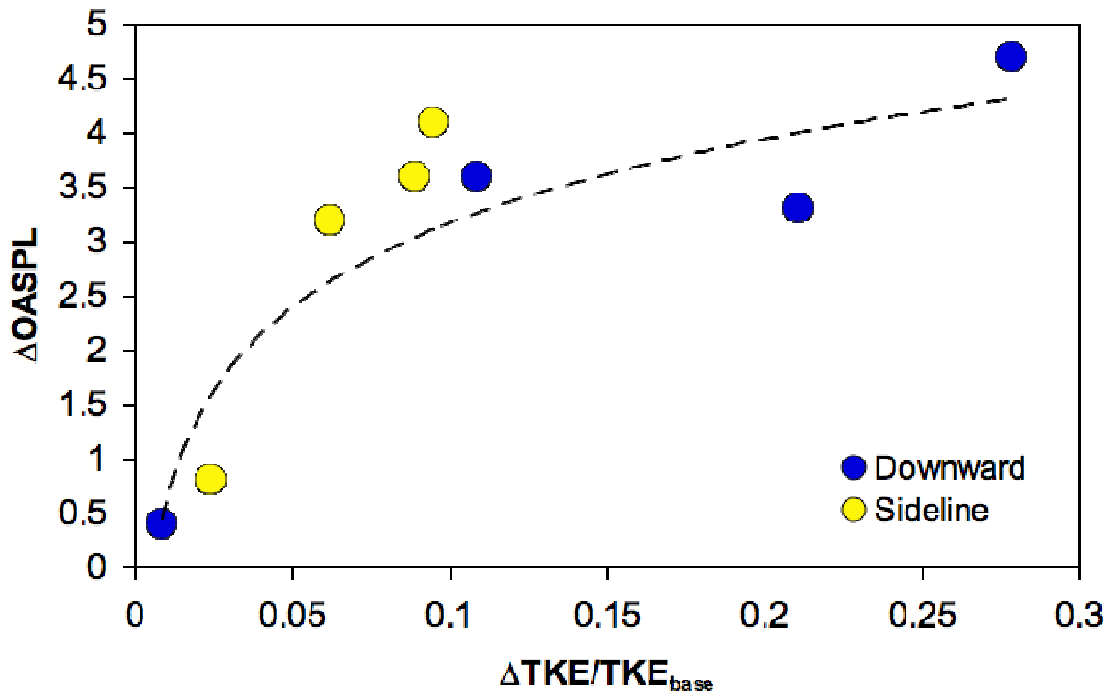


Fig. 26 Correlation between reduction in peak overall sound pressure level (OASPL) and normalized turbulent kinetic energy (TKE).